

RESEARCH ARTICLE

10.1002/2014JF003095

Key Points:

- A high-resolution land cover map is presented
- A new erodibility map is presented
- Dust sources have high spatial and temporal variability

Correspondence to:

Z.-L. Yang,
liang@jsg.utexas.edu

Citation:

Parajuli, S. P., Z.-L. Yang, and G. Kocurek (2014), Mapping erodibility in dust source regions based on geomorphology, meteorology, and remote sensing, *J. Geophys. Res. Earth Surf.*, 119, doi:10.1002/2014JF003095.

Received 26 JAN 2014

Accepted 1 SEP 2014

Accepted article online 4 SEP 2014

Mapping erodibility in dust source regions based on geomorphology, meteorology, and remote sensing

Sagar Prasad Parajuli¹, Zong-Liang Yang¹, and Gary Kocurek¹¹University of Texas at Austin, Jackson School of Geosciences, Austin, Texas, USA

Abstract Mineral dust in the atmosphere has implications for Earth's radiation budget, biogeochemical cycles, hydrological cycles, human health, and visibility. Currently, the simulated vertical mass flux of dust differs greatly among the existing dust models. While most of the models utilize an erodibility factor to characterize dust sources, this factor is assumed to be static, without sufficient characterization of the highly heterogeneous and dynamic nature of dust source regions. We present a high-resolution land cover map of the Middle East and North Africa (MENA) in which the terrain is classified by visually examining satellite images obtained from Google Earth Professional and Environmental Systems Research Institute Basemap. We show that the correlation between surface wind speed and Moderate Resolution Imaging Spectroradiometer deep blue aerosol optical depth (AOD) can be used as a proxy for erodibility, which satisfactorily represents the spatiotemporal distribution of soil-derived dust sources. This method also identifies agricultural dust sources and eliminates the satellite-observed dust component that arises from long-range transport, pollution, and biomass burning. The erodible land cover of the MENA region is grouped into nine categories: (1) bedrock: with sediment, (2) sand deposit, (3) sand deposit: on bedrock, (4) sand deposit: stabilized, (5) agricultural and urban area, (6) fluvial system, (7) stony surface, (8) playa/sabkha, and (9) savanna/grassland. Our results indicate that erodibility is linked to the land cover type and has regional variation. An improved land cover map, which explicitly accounts for sediment supply, availability, and transport capacity, may be necessary to represent the highly dynamic nature of dust sources in climate models.

1. Introduction

Mineral dust in the atmosphere has a wide range of implications for climate, environment, and public health. Dust directly influences the Earth's radiation budget by scattering and absorbing shortwave and longwave radiation [Sokolik and Toon, 1996; Miller and Tegen, 1998; Mahowald *et al.*, 2006]. The Intergovernmental Panel on Climate Change has identified dust as a radiative forcing agent in its climate change reports and considered it as a climate change variable [Intergovernmental Panel on Climate Change, 2007]. Dust also has an indirect effect on climate by modifying cloud microphysical properties by forming cloud condensation nuclei and ice nuclei. Recent studies have linked dust originating from the Sahara to precipitation in the western United States [Creamean *et al.*, 2013] and to cloud formation over western Europe [Bangert *et al.*, 2012]. Dust is linked to the transmission of human and crop diseases and can transport plant nutrients such as iron- and phosphorous-rich minerals through large dust storms [Kellogg and Griffin, 2006].

Existing dust models weakly represent the spatiotemporal variability of dust sources. Accurate identification of dust sources, however, can be very complex and involves understanding the properties of surface features including land cover, geological setting, and chemical/physical composition of the underlying soil. The interaction of these surface features with environmental or meteorological variables further complicates the identification of dust sources. Accuracy of dust emission modeling also depends upon the accuracy of the input data and forcing data (mainly wind) and the way these input data are treated in the models. For example, soil data used for most climate models come from a coarse-resolution ($1^\circ \times 1^\circ$) soil map of the Food and Agricultural Organization. This map was originally derived by Zabler [1999] who compiled information from about 15,000 records at a 1:5,000,000 scale. Dust emission results from models using this soil map show that dust sources are generally well represented in clay-rich areas but not in areas with a low clay content [Crouvi *et al.*, 2012]. An additional constraint in modeling is the "lumped" treatment of the bare soil fraction in these models. For example, in the Community Land Model (CLM), the grid cell for the bare soil fraction available for dust emission is calculated by masking the fraction of vegetation, snow, wetland, and lake based

upon albedo and NDVI (normalized difference vegetation index) threshold [Lawrence and Chase, 2007] derived from Moderate Resolution Imaging Spectroradiometer (MODIS) 1 km data. However, it is obvious that the bare soil fraction, in reality, consists of a number of land cover types that must be resolved at subgrid scales to accurately represent the variability of dust sources. The accuracy in determining soil moisture also constrains the performance of the models because soil moisture determines the threshold friction velocity for a surface. In CLM, soil moisture is calculated by the model as volumetric soil moisture in the top soil layer, but these values have shown lower variability than soil moisture measured in the field [Oleson *et al.*, 2008].

Satellite data sets such as aerosol index (AI) derived from Total Ozone Mapping Spectrometer (TOMS), and aerosol optical depth (AOD) derived from MODIS have greatly contributed to our understanding of dust sources. To account for the common mismatch between observed dust sources in satellite images and modeled dust sources, a factor of *erodibility* has been introduced into dust models as a constraint. Erodibility is commonly defined as the soil erosion efficiency of a surface under given meteorological forcing [Zender *et al.*, 2003]. Surface erodibility has been characterized as uniform, topographic, geomorphic, and hydrologic based upon contrasting assumptions. Uniform erodibility assumes that all bare surfaces are equally erodible. Topographic erodibility assumes that topographic depressions are the largest sources of dust [Ginoux *et al.*, 2001]. Geomorphic and hydrologic erodibility express erodibility as a function of upstream catchment area and upstream flow, respectively [Zender *et al.*, 2003]. Zender *et al.* [2003] demonstrated that all of these erodibility assumptions generally identify the global dust sources with some regional differences, but the geomorphic and topographic erodibility produce the closest overall agreement with observations. The geomorphic and hydrologic erodibility tend to be biased in ocean-draining basins because of the difficulty in resolving the smaller-scale drainage channels at a coarse-resolution mapping [Zender *et al.*, 2003]. It should also be noted that these characterizations of erodibility do not directly represent agricultural areas as anthropogenic dust sources.

Because the existing erodibility concepts reflect the probability of sediment accumulation in a basin, these actually represent the potential “sediment supply” of the land surface rather than “erodibility.” Our erodibility mapping technique is based upon the observed relationship between wind and dust, so the resulting map gives a more literal sense to erodibility. We quantify erodibility using the maximum observed correlation between wind and dust, which is generally observed in the driest season of the year. Any correlation coefficient lower than this maximum value would represent the local environmental effect due to variation in soil moisture, vegetation presence, and crusting.

Aerosol optical properties obtained from satellite instruments such as TOMS and MODIS have been used to calibrate surface erodibility and evaluate the performance of dust models. For example, topographic erodibility was tuned to match the dust distribution observed by TOMS satellite [Ginoux *et al.*, 2001]. Satellite observations, however, have some limitations that result in false identification of dust sources in some areas. One such area is where persistent dust transport/deposition takes place, and another is where pollution/biomass burning contributes significantly to the total dust load [e.g., Schepanski *et al.*, 2012; Parajuli *et al.*, 2013]. Some efforts have been made recently to improve dust source characterization by eliminating these false dust source areas. For example, Ginoux *et al.* [2012] mapped dust sources using high-resolution MODIS level 2 AOD data in conjunction with the land-use map. They applied a filter criterion based upon a threshold Angstrom exponent and single-scattering albedo to distinguish the fine-mode dust. Although this threshold-based approach identifies dust sources in most of the areas, it has some limitations, especially in the areas of long-range transport and biomass burning. This approach can also underestimate actual dust sources by removing some soil-derived fine dust. One example of persistent, long-range dust transport and deposition is seen over the Atlantic in summer and winter, where the dust is carried from Western Sahara [McTainsh, 1980; Koren *et al.*, 2006]. Similar seasonal dust transport takes place over the Arabian Peninsula by Shamal winds originating from the Tigris-Euphrates basin [Reid *et al.*, 2008].

In this work, we present a high-resolution land cover map for the region of the Middle East and North Africa and attempt to quantify erodibility of mapped land cover types. Our approach follows that of Bullard *et al.* [2011] and Lee *et al.* [2011] in which the potential for dust emission from a surface is directly linked to the surface geomorphology, grain size, and land use for a given meteorological condition. As developed by Bullard *et al.* [2011], the conceptual framework for this approach considers (1) the supply of a suitable grain size for dust emission (sediment supply), (2) the availability of that supply owing to factors such as vegetation

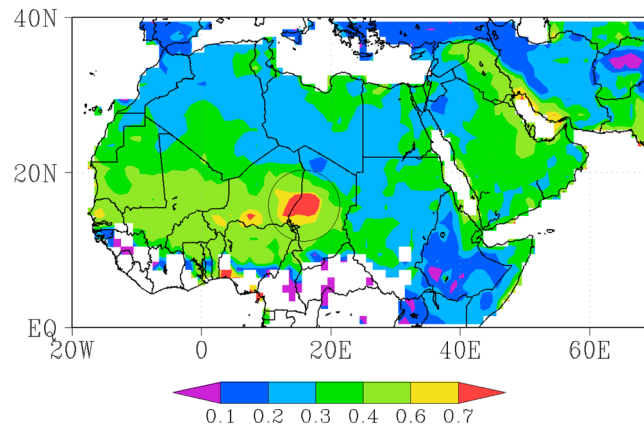


Figure 1. Ten year (2003–2012) mean deep blue aerosol optical depth (AOD) over the study domain. The well-known dust source (Bodélé) is marked by the black circle.

associated with transported dust and by including agricultural dust sources compared to existing erodibility maps. Quantification of erodibility of different land cover types enables representation of the spatiotemporal dynamics of dust sources in climate models.

2. The Study Area

The Middle East and North Africa (MENA) region contains many dust sources or “hot spots,” contributing more than 50% of total global dust emission. MENA dust sources share characteristics with dust sources globally. Most are located in arid and semiarid regions and are characterized by geographic depressions or playas (dry lakes) and proximity to highlands [Prospero *et al.*, 2002]. Prospero *et al.* [2002] identified dust sources globally by developing an aerosol index (AI) using the backscattered ultraviolet radiance at 0.340 and 0.380 μm wavelengths of TOMS onboard NIMBUS 7. The major sources of dust in the MENA region are located within the Tigris-Euphrates alluvial plain in Iraq/Kuwait, the low-lying flat lands along the Persian Gulf, the Ad Dahna and Rub’ al Khali deserts, the Bodélé depression in Chad, the Sistan basin bordering Pakistan and Afghanistan, and basins of Zuphar and Al Hazhar mountains in Oman/Yemen [Prospero *et al.*, 2002; Reid *et al.*, 2008].

The generation of atmospheric dust in the MENA region has been associated with two monsoon winds. The first is the Shamal (low-level hot, dry, northwesterly wind) prevalent in the Middle East, and the second is the Harmattan (low-level hot, dry, northeasterly wind) prevalent in North Africa. The Shamal winds are most active during summer and cause large dust storms known as “Haboob,” which show a recurring seasonal pattern and origin. The Shamal winds originate from the northwest of the Middle East region and are channelized into the Persian Gulf by the mountains of Turkey/Iraq to the northeast and the high plains of Saudi Arabia to the southwest [Rao *et al.*, 2003]. These winds usually extend over a wide region and affect several countries including Iraq, Kuwait, Bahrain, Saudi Arabia, United Arab Emirates (UAE), and Oman. In North Africa, the Harmattan winds are active during the winter and early spring and carry dust originating from Western Sahara across the Atlantic [McTainsh, 1980; Koren *et al.*, 2006]. Harmattan dust storms reduce visibility, destroy crops, and affect daily life in many countries including Nigeria, Burkina Faso, Ghana, Niger, Mali, and Guinea. Many dust events in the MENA region are also associated with regional atmospheric circulation [Engelstaedter and Washington, 2007], while others are linked to cyclones, fronts, or thunderstorms [Prospero *et al.*, 2002].

Figure 1 shows the 10 year (2003–2012) mean AOD at 550 nm over the study area obtained from level 3.0 daily MODIS Aqua deep blue AOD (MYD08_D3) product at ($1^\circ \times 1^\circ$) resolution. Deep blue MODIS AOD is derived for cloud-free days over bright reflecting surfaces using the advantage that surface reflectance is low in blue channels [Hsu *et al.*, 2004]. Although this map shows the general distribution of observed dust in the atmosphere, it does not necessarily indicate the dust source distribution. Bodélé ($\sim 16.5^\circ\text{N}$, 16.5°E) is a year-round active dust source [Prospero *et al.*, 2002; Koren *et al.*, 2006], which is evident in Figure 1. Bodélé is

and moisture level (sediment availability), and (3) the transport capacity of the wind as measured by wind energy (transport capacity). This conceptual framework parallels to that developed for aeolian dune fields [Kocurek and Lancaster, 1999]. Based on this framework, we first classify the study area into several key land cover categories by visually examining high spatial resolution images. We then quantify their erodibility using the maximum observed correlation between reanalysis wind speed and satellite retrieved AOD. This approach improves dust source characterization by eliminating false dust sources

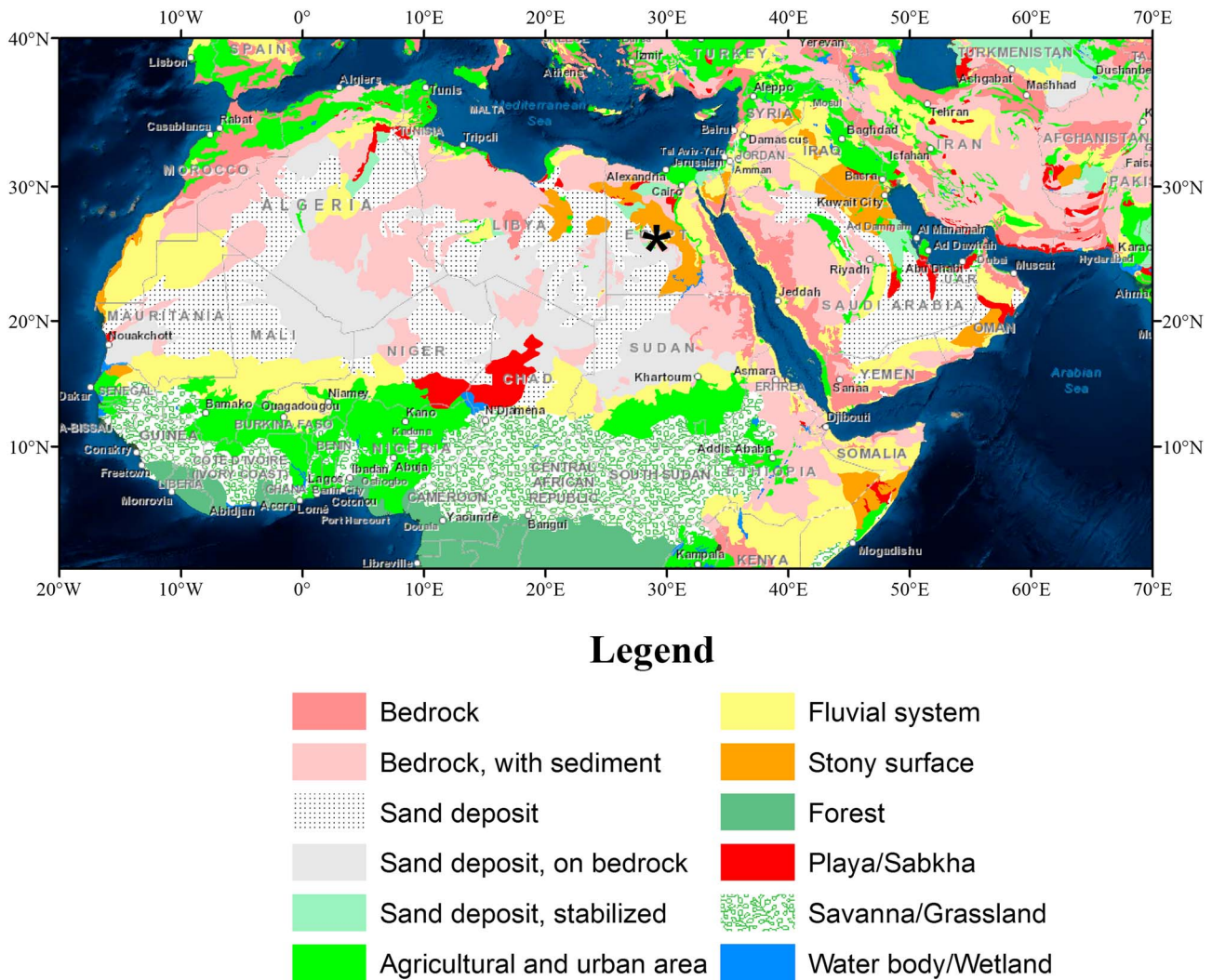


Figure 2. Land cover map of the study area developed by visually examining the high-resolution images from Google Earth Professional and ESRI Basemap. A zoom in of the area marked by the star is presented in Figure 3.

an ideal location for dust emission because of its unique geographic location, sustained high winds, high sediment supply/availability, and proximity to sand dunes.

3. Methods

3.1. Land Cover Mapping

We used high-resolution red, green, and blue images obtained from ArcGIS/Basemaps and Google Earth Professional, in which resolution ranges from 1 m to several meters depending upon the location. We mapped the land cover types by visually examining these images at a scale of 1:250,000, in which land cover features such as sand dunes, settlements, and agricultural areas were clearly distinguishable (Figure 3). Figure 3 shows a zoom-in image (a) and the mapped polygons (b) of a typical location in Egypt (marked by a star in Figure 2) at 1:250,000 scale, where multiple land cover types are present in a small area. Our mapping technique is subjective to the extent that the land cover is classified by the viewer, but in our experience, most geomorphic features are clearly distinguishable in these images except in a few areas described later.

We also attempted to classify the study area using automatic image classification methods such as the maximum likelihood method available in ArcGIS. Similar automatic image classification techniques have been used in the past for land cover/land surface mapping [Hansen et al., 2000; Loveland et al., 2000; Ballantine et al., 2005].

Identification of a land cover type in the high spatial resolution images involved frequent zoom in of the area at full resolution. Identification of land cover type was difficult in some areas, especially where the image was unclear (e.g., areas having persistent cloud cover and high albedo) or when full-resolution image was not available. Additionally, some land cover types were complex mixtures of different land cover types. In these situations, we used a number of secondary sources to classify the land cover, especially published regional descriptions [e.g., *Lobeck, 1946; Goudie, 2013*]. The erodibility map by *Ginoux et al. [2012]* and dust source map by *Prospero et al. [2002]* provided the general distribution of hot spots of dust sources, which was the basis for focusing our study in the MENA region. Although our land cover classification was inspired by all of these previous studies, the final land cover types are closest to those erected by *Bullard et al. [2011]*.

About 1500 polygons were created in the study area by identifying and classifying the landforms in ArcGIS. In order to avoid creating too many types, transition zones were classified according to their closest type. The polygons were then grouped into 12 land cover types of which three are nonerodible: bedrock, forest, and water body/wetland. Overall, the determination of the number of types is a balance between the identification of land covers in a diverse terrain and the distillation of these into a workable number of types for regional model input.

3.2. Determination of Erodibility

We calculated the correlation coefficient between surface wind speed and satellite-retrieved AOD using historical data (2003–2012) because we hypothesize that the strength of the correlation between wind speed and atmospheric dust concentration can be used as a proxy for surface erodibility.

MODIS deep blue data [*Hsu et al., 2004*] were chosen because these data sets have been widely validated against field and Aerosol Robotic Network measurements [*Hsu et al., 2004; Ginoux et al., 2012*]. MODIS deep blue data are especially useful for studying dust sources because the data are available even over bright deserts where many other satellite-based algorithms fail to retrieve dust. One of the limitations of MODIS AOD, however, is that it only represents the noontime dust, which can underestimate some dust sources [*Schepanski et al., 2012*]. Level 3 deep blue MODIS AOD data are available daily at ($1^\circ \times 1^\circ$) spatial resolution from 2002 to the present. We used level 3 data to better match the resolution of reanalysis wind data, although higher-resolution level 2 deep blue data ($0.1^\circ \times 0.1^\circ$) are available. Reanalysis data such as National Centers for Environmental Prediction/National Center for Atmospheric Research (NCEP/NCAR) Reanalysis 1 and ERA-Interim Reanalysis are often regarded as observations because a large number of ground-based and satellite observations are assimilated in generating these reanalysis outputs. NCEP/NCAR reanalysis data have $2.5^\circ \times 2.5^\circ$ resolution, and ERA-Interim have $1.5^\circ \times 1.5^\circ$ resolution, and so both were regridded to ($1^\circ \times 1^\circ$) to match the resolution of MODIS grid. We extracted the winds from reanalysis data at 12 noon (geomagnetic time (GMT)), which is the closest time to MODIS AOD retrieval (01:30 P.M., local time).

Accuracy of the surface wind speed used is critical to our approach. In order to identify the best available data and to understand the grid-scale wind-dust relationship, we examined how well the NCEP [*Kalnay et al., 1996*] and ERA-Interim [*Dee et al., 2011*] surface winds correlate with MODIS AOD at Bodélé, Chad. We plotted the scatter diagram between 1000 hPa wind speed and MODIS AOD taking the closest pixel to Bodélé. Both ERA-Interim and NCEP data sets had 3332 observations after eliminating missing data corresponding to cloudy days in MODIS data. Preliminary results (see section 4.2) showed that the ERA-Interim data were much better correlated with MODIS deep blue AOD at Bodélé, so we only used ERA-Interim data for further analysis.

For mapping the erodibility of the entire study area, we segregated the 10 years of surface wind and AOD data into monthly data and calculated the monthly correlation at each grid cell. Daily data for all 10 years were combined to calculate the monthly correlation. The number of observations at each grid cell available was constrained by the availability of MODIS AOD data for cloud-free days. As the wind-dust relationship is nonlinear, as observed in wind tunnel experiments [e.g., *Shao, 2000*], we calculated Spearman's rank correlation coefficient ρ between MODIS deep blue AOD at 550 nm and ERA-Interim wind speed at 10 m at all grid points. The significance of the obtained correlation is evaluated by calculating corresponding P values at each grid cell, where p is the probability of having a correlation as large as the observed value by random chance.

A low correlation between wind speed and AOD should characterize areas with pollution or biomass burning, as well as areas of persistent dust transport/deposition. Our method, however, should emphasize anthropogenic dust sources from agricultural areas because these are characteristic of the underlying land surface. As noted by

Bullard et al. [2011], agricultural areas are not currently factored into the existing erodibility maps, although these areas have been identified as major dust emission sites by many studies [e.g., *Lee et al.*, 2011; *Ginoux et al.*, 2012; *Van Pelt et al.*, 2013]. Another advantage of our approach is that the association of AOD with surface wind speed makes the correlation less sensitive to the height of dust layer and better identifies soil-derived local dust.

To put our correlation map within the context of the current literature, we referred to *Ginoux et al.* [2012], who examined the dust sources in detail by classifying the dust sources into anthropogenic and natural sources using high-resolution level 2 MODIS AOD data. We also referred to *Engelstaedter and Washington* [2007], who studied the relation between the annual cycle of wind and TOMS AI over North Africa. We use mean monthly wind vectors, precipitation data, and Angstrom exponent data to facilitate discussion of the erodibility map.

3.3. Erodibility of Land Cover Types

After preparing the monthly correlation maps (section 3.2), the maximum of the monthly observed correlation between ERA-Interim 10 m wind speed and deep blue MODIS AOD at each grid cell was used to quantify the erodibility. *Bullard et al.* [2011] discussed a qualitative approach to represent the dust emission potential of different land cover types. They identified land covers having low, high, and medium dust emission potential, which was based upon their knowledge of dust sources and the frequency of dust plumes observed in MODIS images. However, quantification of erodibility is necessary for input to dust/climate models.

In order to ensure the reliability of the erodibility map, we systematically applied some filter criteria and processed the data as described below. First, the grid cells having a statistically insignificant correlation coefficient at 95% confidence level were removed from the maximum of mean monthly correlation map. We then masked the grid cells where mean monthly precipitation was more than 0.5 mm/d, which is considered a typical precipitation rate in the arid regions. We used Global Precipitation Climatology Project (GPCP) version 2.2 Satellite Gauge (SG) combined monthly precipitation data set $2.5^{\circ} \times 2.5^{\circ}$ between 2003 and 2012 for this mask. Further, we eliminated the areas dominated by fine-mode aerosols by removing the pixels which have a mean monthly Angstrom exponent greater than zero, because the coarse-mode local dust typically shows Angstrom exponent close to zero [*Eck et al.*, 1999]. We used MODIS Aqua level 3 mean monthly Angstrom exponent data at 470/660 nm between 2003 and 2012 for this purpose. We also removed the remaining few grid cells which showed negative correlation as they are not characteristic of the underlying land cover. Finally, we masked the nonerodible areas (forest, bedrock, and water body/wetlands). We determined the mean correlation coefficient of each land cover type over the entire study area and its statistics using the resulting erodibility map in section 3.2. The vector-based, land cover map prepared in ArcGIS was converted into a gridded map at $(0.1^{\circ} \times 0.1^{\circ})$ degree using the maximum area method, which yielded 401×876 grid cells over the study area. In order to match the resolution with this gridded map, the erodibility map prepared at $(1^{\circ} \times 1^{\circ})$ resolution was regridded to $(0.1^{\circ} \times 0.1^{\circ})$ resolution by assigning a constant value corresponding to a $(1^{\circ} \times 1^{\circ})$ grid cell to all new finer grids within that grid cell. The mean correlation coefficient for each land cover type was determined by averaging the correlation coefficients over the entire $(0.1^{\circ} \times 0.1^{\circ})$ grid cells corresponding to that particular land cover type. The mean correlation is reported along with its standard deviation, maximum, minimum, and the number of grid cells used.

We referred to *Zender et al.* [2003] for comparison, in which a rigorous comparison of uniform, topographic, geomorphic, and hydrologic erodibility is presented. The topographic erodibility [*Ginoux et al.*, 2001] is most suitable for identifying the improvements in our erodibility map because it was tuned against satellite data.

4. Results

4.1. Land Cover Types

Bedrock, with sediment is the largest class in terms of area, covering about 20% of the study area (Figure 2 and Table 1). This class includes any land cover features that have some sediment deposits lying on the surface of bedrock. Included within this type are high-relief bedrock uplands with incised river channels that contain fine sediment, intermountain areas with sediment deposits (e.g., the Afghanistan/Pakistan border), and structural grabens containing fine sediment (e.g., grabens of north-east Ethiopia [*Lobeck*, 1946]). Finally, this type includes bedrock areas with a discontinuous cover of sediment, such as in northeastern Africa and

Table 1. Number of Polygons, Total Area, and Key Locations of the 12 Land Cover Types in the Study Area

Land Cover Types	Area in km ² (%)	No. of Polygon	Key Locations
Bedrock	2,562,316 (7.65)	182	Atlas mountains, west Saudi Arabia, northeast of Turkey, north of Afghanistan
Bedrock, with sediment	6,815,687 (20.35)	197	Mountains of Iran and Afghanistan, Atlas mountains, Mountains of Tunisia and Libya, Central Algeria, Nubian mountains of Ethiopia, Sudan, Djibouti, Eritrea, and Somalia
Sand deposit	4,135,658 (12.35)	41	Mauritania and north Algeria, southwestern Libya, Rub Al Khali desert of Saudi Arabia
Sand deposit, on bedrock	3,048,532 (9.10)	20	Southern Algeria, eastern Libya, northern Afghanistan
Sand deposit, stabilized	598,705 (1.78)	19	Registan desert and northern Afghanistan, east coast of Kuwait and Saudi Arabia
Agricultural and urban area	5,094,436 (15.21)	513	Sahel region, base of Atlas mountains, Tigris-Euphrates basin, Nile basin, Indus River basin in Pakistan, northern Turkey
Fluvial system	4,267,695 (12.74)	225	Sahel region, southwest of Atlas Mountains, Somalia, Tigris-Euphrates basin, east of lower Nile, northern Iran
Stony surface	1,016,783 (3.04)	36	West coast of Mauritania, Kuwait, western desert of Egypt, central Libya
Forest	1,332,598 (3.98)	10	Rainforest of equatorial Africa
Playa/sabkha	719,153 (2.14)	110	Bodélé depression in Chad, dried lakes of Afghanistan/Pakistan, east coast of Somalia, northeast of Algeria, coastline of the UAE, east coast of Oman
Savanna/grassland	3,730,400 (11.14)	31	West African region between Sahel and tropical rainforest of Africa
Water body/wetland	159,571 (0.48)	153	Scattered
Total	33,481,535	1,515	

western Saudi Arabia where sediments have been deposited from wadis [Lobeck, 1946]. All of these surfaces are similar and classed together because potential dust sources occur as sediment cover over bedrock terrain.

Agricultural and urban area is the type that includes agricultural areas, developed lands, and settlements (Figure 2, and Table 1). We combined the agricultural areas and urban areas for two reasons. First, the urban areas constitute a small fraction of the agricultural areas and they are collocated with the agricultural areas in most places. Second, both of these areas represent “anthropogenic dust sources.” Most agricultural areas are located within fluvial systems or in the vicinity of these systems, occurring on mountain slopes or within valleys. A further subdivision of agricultural areas is possible based upon an arbitrary threshold of relief. High-relief agricultural areas are those where cultivation is on the slope of mountains, which is common in the north of Turkey and Syria. Low-relief agricultural areas are mostly located in broad river valleys with gentler slopes. Examples include the Tigris-Euphrates basin, the lower Nile River basin, and the Indus River basin where the relief is generally less than 300 m. Low-relief agricultural areas are thought to be stronger dust sources than upland agricultural areas because the former house more fine fluvial sediment [Bullard et al., 2011]. Dust emission from agricultural land shows a strong seasonality associated with tilling and irrigation. Although settlements and developed areas cover a small area, these can be strong dust sources because of anthropogenic soil disturbance. In some areas, settlements are on coastal sabkhas where the dust emission potential is high (e.g., coastal area of the UAE). This land cover type has the smallest individual polygon in the entire study area with an area of ~49 m².

Sand deposit represents large areas of aeolian sand dunes and sand sheets within the MENA region, including the sand seas of North Africa and the Arabian Peninsula (Figure 2 and Table 1). This broad class of land surface has been broken into three types: (1) sand deposit where dunes appear active and the surface is largely covered by sand at image resolution, (2) sand deposit, stabilized, where dunes appear inactive, vegetated, or otherwise largely stabilized, and (3) sand deposit, on bedrock, where the bedrock is visible between dunes (Table 1 and Figure 2). The general location of major sand deposits in the North Africa is consistent with that of Ballantine et al. [2005]. In general, active sand dunes are considered poor sources of dust, but recent work suggested that dust-sized particles are produced by aeolian abrasion of sand particles [Crouvi et al., 2012]. Stabilized dunes commonly house dust, which may be emitted with dune reactivation [Bullard et al., 2011]. Sand saltation is thought to be a prime driver for dust emission; thus, any fine-grained areas (i.e., fluvial, playa deposits) within areas of sand deposits may be readily deflated [Prospero et al., 2002].

Fluvial system is any hydrologic basin characterized by a network of small streams draining toward a lower elevation. This class forms the third largest type of land cover, accounting for 13% of the study area (Figure 2 and Table 1). In mapping this type, the entire catchment area was included, regardless of whether the systems are currently active or are relict geomorphic features. We also include within this type coastal deposits formed from fluvial sediments (i.e., deltas, beaches), which constitutes a tiny fraction of the total area mapped.

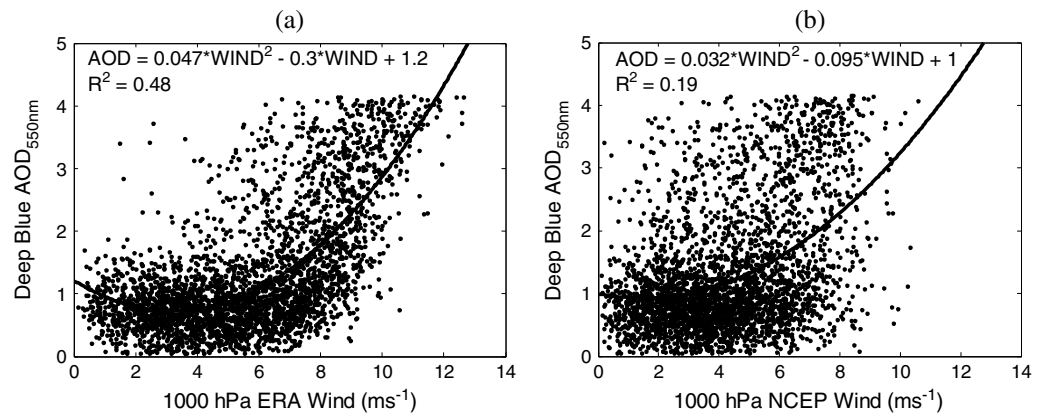


Figure 4. Scatterplot between MODIS deep blue AOD at 550 nm and (a) ERA-Interim reanalysis wind speed (ms^{-1}) at 1000 hPa, (b) NCEP reanalysis 1 wind speed (ms^{-1}) at 1000 hPa. The data points represent about 3332 daily observations between 2003 and 2012 at Bodélé, Chad. The wind speed data are retrieved at 12:00 GMT from 6-hourly data to match the MODIS data retrieval time (01:30 PM local time).

Some fluvial systems are also commonly mixed with agricultural land and sabkhas. The availability of fine sediment within the fluvial system depends upon factors such as source area material, degree of weathering, and current energy. *Bullard et al.* [2011] subdivided fluvial systems into (1) high-relief systems in mountainous regions, which are typically coarser grained, and (2) low-relief systems with common broad floodplains, which typically house significant fine sediment. The Sahel, forming the transition zones between the Sahara Desert to the north and savanna to the south, is mainly characterized by fluvial systems but includes stabilized sand dunes, savannas, agricultural areas, and settlements. The Sahel fluvial systems are also identified in the landform map developed by *Ballantine et al.* [2005]. Dust emission from the Sahel is strongly affected by soil moisture variation. Figure 7 clearly shows that this region receives relatively higher precipitation in the summer associated with the West African monsoon. Other key fluvial systems are located in the southwest of the Atlas Mountains, the Tigris-Euphrates River basin, and Somalia. The availability of fine sediment in this type largely depends upon the nature of the fluvial sediment load and any periodic drying.

Stony surface or reg in the MENA region largely occurs as wind deflated terrains characterized by gravel, yardangs, and small dunes (Figure 2 and Table 1). Generally, fine sediment has been deflated from these surfaces. This land cover type is mainly found in Western Sahara and the western desert of Egypt. This type is also found in the Negev Desert in Israel, which is a part of an ancient alluvial system [*Matmon et al.*, 2009].

Playa/sabkha include ephemeral lakes, playas, chotts, pans, and coastal sabkhas. In the MENA region, these features only cover about 2% of the area (Figure 2 and Table 1). Most of these features appear bright white in satellite images. Most sabkhas are flats containing salts such as halite (NaCl) and gypsum ($\text{CaSO}_4 \cdot 2\text{H}_2\text{O}$) [*Goudie*, 2013]. Some sabkhas within the MENA region are also cultivated. Major sabkhas are near coastal regions, the most prominent being that in the UAE, which is heavily affected by anthropogenic activities. Playas and sabkhas are commonly regarded as major sources of dust.

Savanna/grassland is the typical land cover between the Sahel and the African rainforest (Figure 2 and Table 1). These areas appear as an east-west strip between 5 and 13°N, which is consistent with the global land cover map developed by *Loveland et al.* [2000]. Although vegetation generally protects the surface from erosion, disturbances such as grazing, burning, and other human activities can make these areas susceptible to erosion. These areas are specially characterized by high biomass burning [*Bond et al.*, 2013], yielding a complex mixture of aerosols over the region. High Angstrom exponent values seen over this region (Figure 7) also confirm this because biomass burning aerosols are generally characterized as fine-mode aerosols.

Bedrock, forest, and water body/wetland form land cover types of no practical dust emission (Figure 2 and Table 1). We define bedrock as any hard surfaces lacking fine sediment irrespective of the relief, although most of the areas in this type have high relief. Some of the largest mountains in the MENA region such as the Atlas Mountains, west Arabian Mountains, and mountains in Iran/Afghanistan lie in this category. Volcanic formations are also included in this category, such as the Tibesti Mountains in Chad and the Jebel Marra

Mountains in Sudan. We include yardangs in this category. Some of the largest yardangs are located in the Lut Desert of Iran, central Sahara, and the Mut Desert, Egypt [Goudie, 2013]. Some rocky plateaus such as the Tassili n'Ajjer Mountains in Algeria are also included in this category. Forest is the typical feature of equatorial Africa, commonly known as rainforest, and is clearly seen in the global land cover map developed by Loveland *et al.* [2000]. Water body/wetland features constitute a very small area of the MENA region.

4.2. Erodibility

Figure 4 shows the scatterplot between MODIS deep blue AOD at 550 nm and reanalysis surface winds at 1000 hPa for Bodélé (16.5°N, 16.5°E). The scatterplot shows that ERA-Interim wind speed is better correlated with AOD compared to NCEP wind speed. The scatter diagram also shows that the wind-dust relationship is nonlinear as expected. The power relationship observed between wind speed and AOD at a coarse grid scale is consistent with wind tunnel observations. In wind tunnel observations, vertical dust flux is found to be proportional to some power of friction speed, where the power varies from 2 to 5 [Shao, 2000].

Although the quadratic best fit line in Figure 4 explains a large fraction of variance in determining the AOD, there is a considerable scatter in the data, which we ascribe to several factors. First, there is some time mismatch between MODIS data and reanalysis wind data as noted in section 3.2. Second, dust at Bodélé may also be contaminated by dust and pollution transported from surrounding areas. Third, the reanalysis wind consists of 6-hourly means, which may not adequately represent the wind gusts responsible for dust emission. Fourth, it should be noted that there is uncertainty involved in MODIS and reanalysis wind data retrieval itself. Lastly, small-scale dust plumes and wind gusts may not be represented very well at (1° × 1°) resolution. Nevertheless, the trend evident in Figure 4 and the moderate correlation between two completely independent data sets suggests that ERA-Interim wind and AOD data can be used for quantifying land cover erodibility.

Figure 5 shows the resulting map of Spearman's correlation between ERA-Interim wind at 10 m and MODIS AOD at 550 nm prepared at (1° × 1°) resolution. Pearson's correlation showed identical dust source distribution (not shown). The map well represents the annual cycle of dust source mobilization in the study area. *P* values corresponding to the correlation at each grid cell are presented in Figure 6. It can be seen that most of the erodible areas of our interest have significant correlation at the 95% confidence level. Most of the areas showing insignificant correlation are either nonerodible areas or the areas that are affected by long-range transport and biomass burning. The correlation map shows that the dust emission has seasonal dynamics. Wind erosion is strongest in the winter (December-January-February (DJF)) as indicated by the bright pink color. The Bodélé depression (~16.5°N, 16.5°E) is active throughout the year but less active in summer (June-July-August-September), which is explained by the precipitation associated with the African monsoon (Figure 7). The dust source in the horn of Africa (Somalia) (~8°N, 45°E) is active in most months except March, April, November, and December. The dust source in the Tigris-Euphrates basin (~30°N, 47°E) shows high seasonal variability. This area is active during all other months except in August, September, November, and December. Similarly, dust sources in the Afghanistan/Pakistan border (~30°N, 62°E) are active throughout the year, but the area of dust emission reduces in summer.

Engelstaedter and Washington [2007] studied the relation between wind and dust by plotting Spearman's rank correlation between the annual cycle of wind and TOMS AI. They did not observe a strong positive correlation at Bodélé but at a location northeast of Bodélé. However, we clearly see a strong correlation between wind speed and AOD at Bodélé in all seasons although it is weak in summer. This discrepancy may be explained by two reasons. First, deep blue AOD is a more quantitative indicator of dust, whereas TOMS AI used in their study is more qualitative [Ginoux *et al.*, 2012]. Second, the TOMS AI is more sensitive to the height and type of aerosols [Torres *et al.*, 1998]. There are many areas where there is a strong negative correlation between wind speed and dust in our correlation map (Figure 5), which also varies seasonally. A strong negative correlation is seen over Ethiopia south of lake Abbe, Sudan near Khartoum, and Kenya in most of the seasons. Close examination of these areas revealed that these areas are characterized by savannas over elevated topography. Clearly, these areas are not the sources of dust. High Angstrom exponent values seen over this area (Figure 7) also suggest dominance of fine-mode aerosols. Wind vectors in these areas (Figure 7) show that the wind speed is very low, which support our idea that the negatively correlated areas do not represent the local dust mobilization. A similar negative correlation is observed over Algeria and Libya in the summer (June-July-August), which is also characterized by reduced wind speed. Engelstaedter and Washington

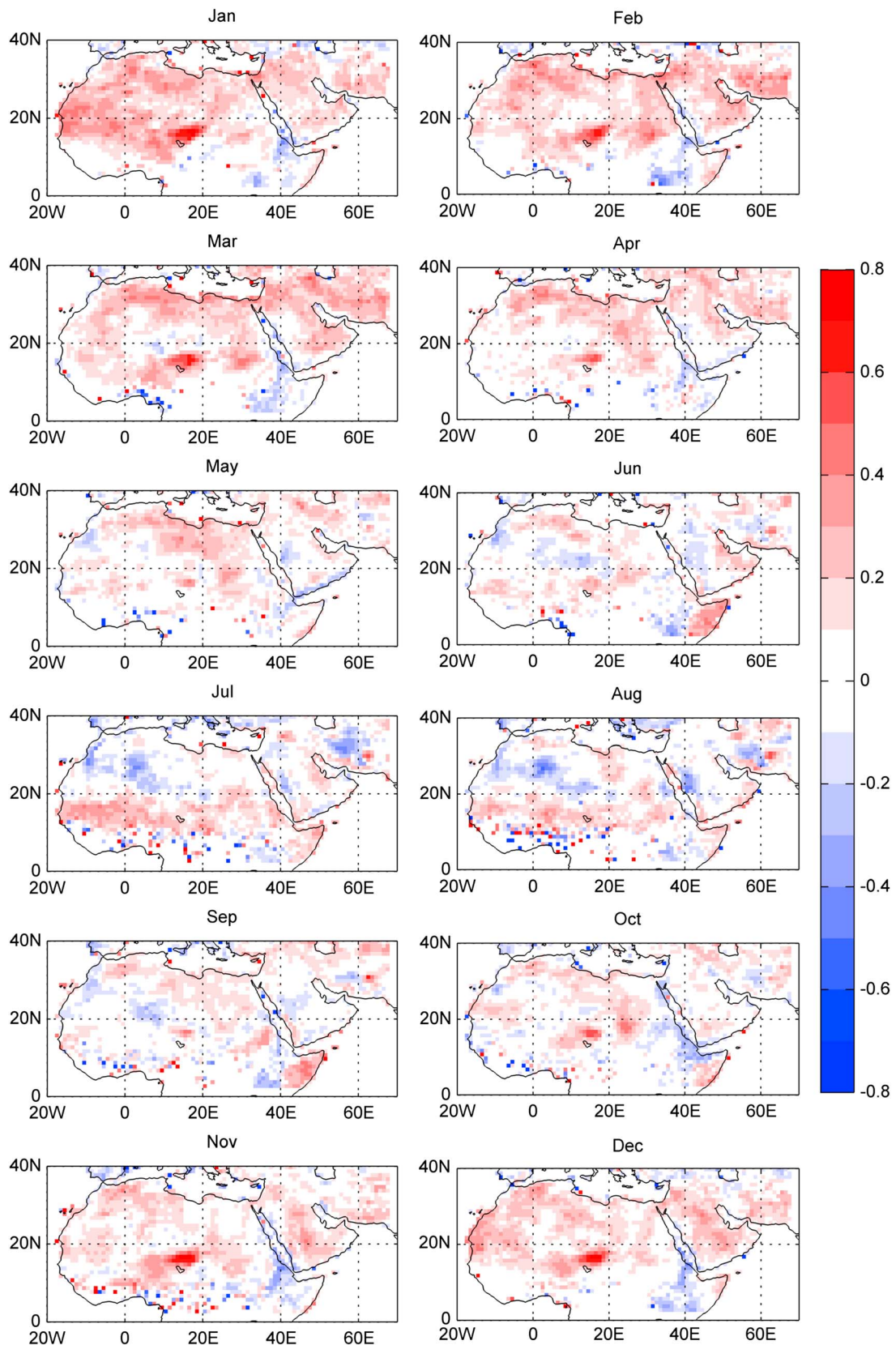


Figure 5. Monthly correlation map between ERA-Interim wind at 10 m and MODIS deep blue AOD at 550 nm using historical data of 10 years (2003–2012). *P* values corresponding to this correlation map are presented in Figure 6.

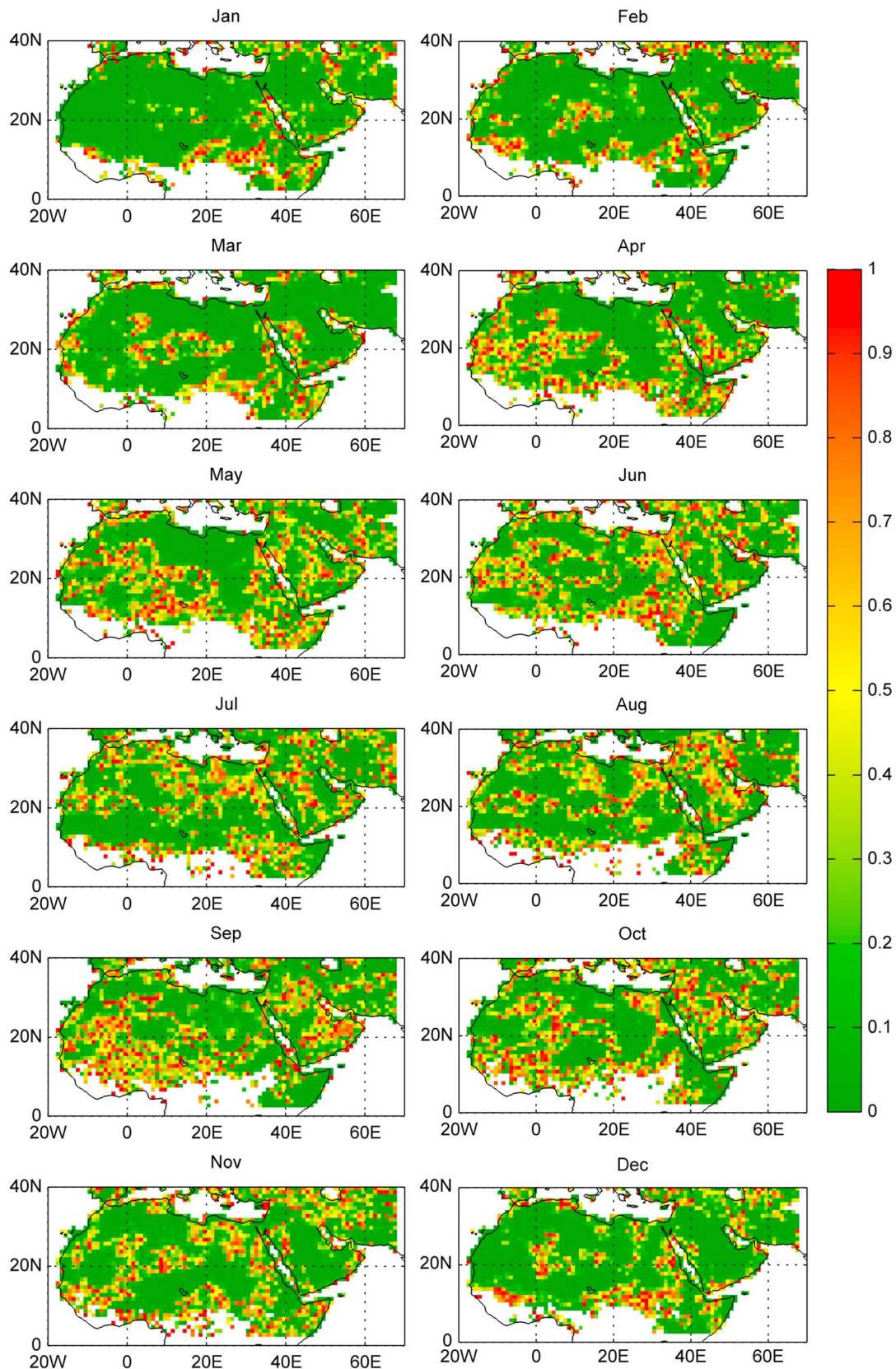


Figure 6. Map of P values corresponding to the correlation map in Figure 6, where P is the probability of getting the correlation as large as the observed correlation by random chance.

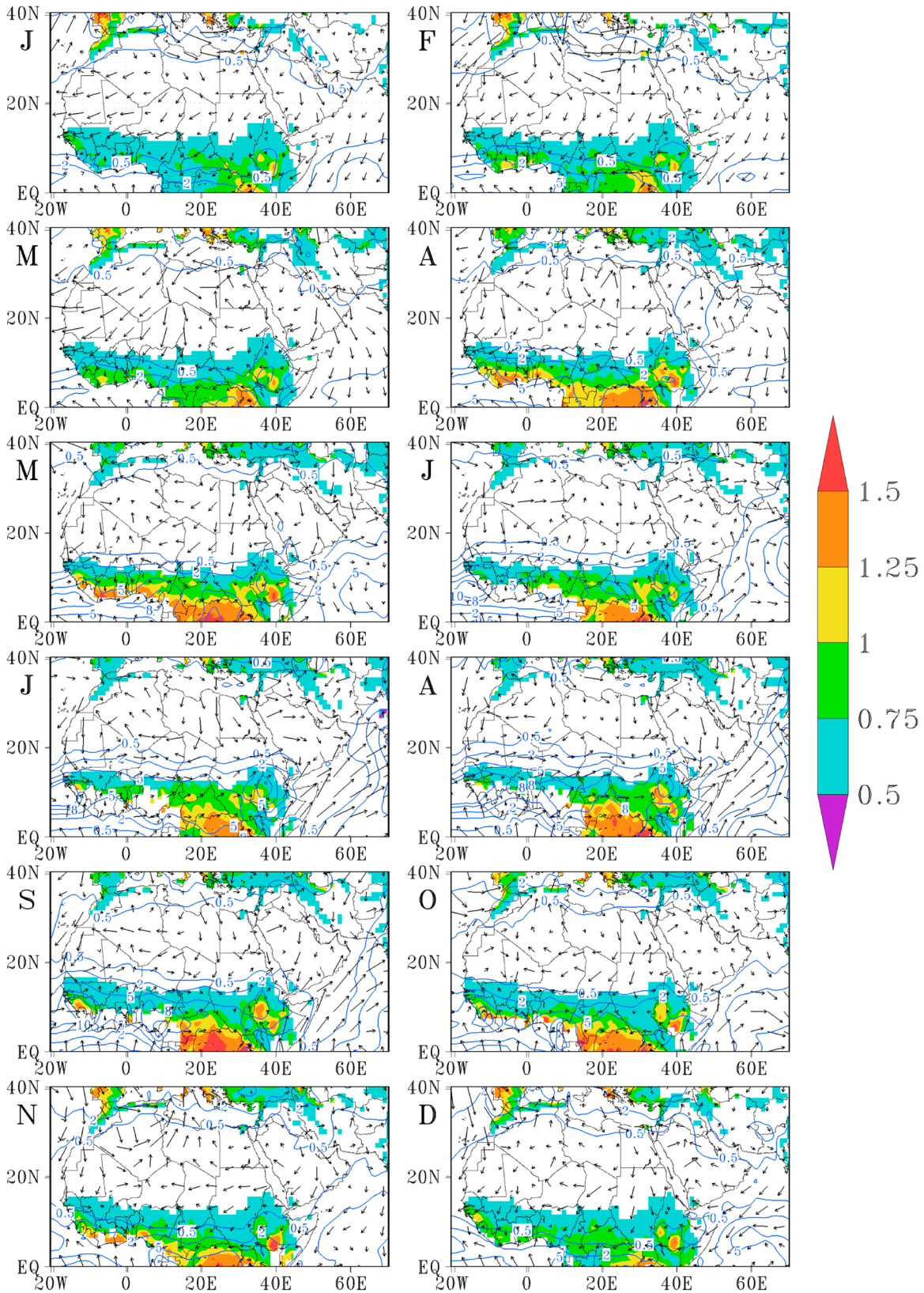


Figure 7. ERA-Interim 10 m wind vectors (arrows), GPCP mean precipitation (contours), and Angstrom exponent at 470/660 nm (shaded). ERA-Interim wind vector represents mean monthly wind speed (m/s) and direction at 12 GMT for 2003–2012. Precipitation data are monthly mean (mm/d) derived from GPCP version 2.2 SG data set for 2003–2012. Angstrom exponent data are monthly mean derived from MODIS Aqua level 3 product for 2003–2012.

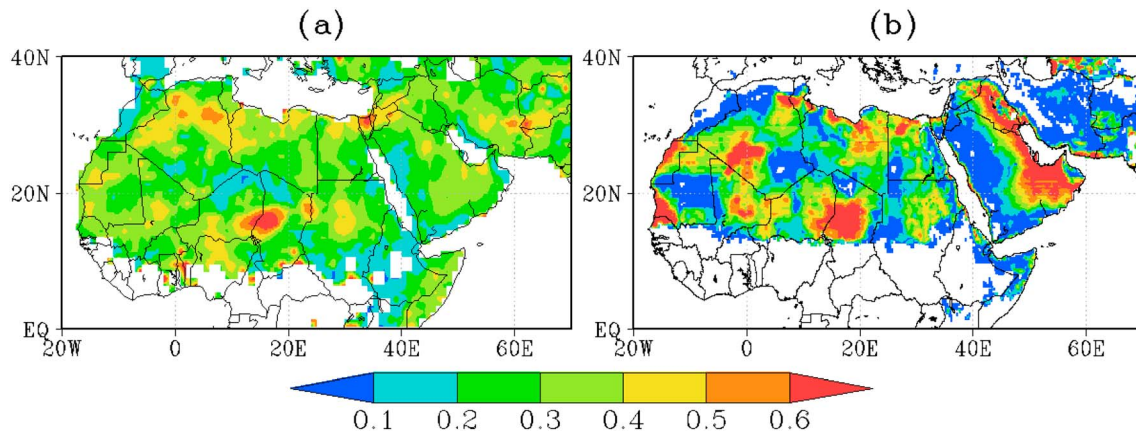


Figure 8. (a) Our erodibility map based upon the correlation between ERA-Interim 10 m wind and MODIS AOD at 550 nm. (b) Topographic erodibility map developed by *Ginoux et al.* [2001].

[2007] related the negatively correlated areas to the zones of strong convergence, which favors dust transport at high altitude.

Ginoux et al. [2012] showed that dust sources represented by coarse-mode dust (represented by dust optical depth separated from fine-mode dust) distribution dominates in spring and summer, especially over the Sahel area. Our results, however, show that the dust source mobilization is strongest in January, February, and March. High dust optical depth seen by *Ginoux et al.* [2012] in spring and summer may reflect the contamination of dust by transported dust and biomass burning aerosols as shown by high Angstrom exponent values over this area (Figure 7). High dust mobilization is seen over Saudi Arabia and Tigris-Euphrates river valleys in spring (March-April-May) in both of the maps. However, mobilization in these areas is very strong in winter (DJF) as well in our correlation map, which is not seen in their map.

The resulting erodibility map based on the maximum mean monthly correlation at each grid cell is presented in Figure 8a. The topographic erodibility map proposed by *Ginoux et al.* [2001] is presented in Figure 8b for direct comparison. Our map appears to reduce the overall dust source strength compared to the topographic erodibility map. In the areas where dust transport is dominant, our map improves the dust source characterization as expected. For example, the topographic erodibility map and the mean AOD map (Figure 1) show the Arabian Peninsula, especially in the UAE, to be highly erodible. However, the high erodibility seen in the topographic erodibility map over the Arabian Peninsula actually reflects the dust transported by the Shamal wind from a dust source within the Tigris-Euphrates basin [*Reid et al.*, 2008]. The land cover map (Figure 2) shows that this area is a mixture of sabkhas, sand deposits, stony surfaces, and fluvial systems. Our map modulates the source strength in these areas because the surface wind shows a weaker correlation with the Shamal wind transported dust, which is advected mostly in the middle/upper troposphere. In this area, the geomorphic and hydrologic erodibility maps better match with our erodibility map. The agricultural area in the Sahel region and Tigris-Euphrates River basin is seen as highly erodible in our map, which is also identified in all topographic, hydrologic, and geomorphic erodibility maps. The land cover map (Figure 2) shows extensive agricultural practice in these areas indicating enormous anthropogenic dust potential. Our map correctly emphasizes the dust source in the Afghanistan/Pakistan border region where playas and fluvial deposits are abundant, as discussed in section 4.1. Hydrologic and geomorphic erodibility maps better match with our erodibility map in this region. In our map, strong erodibility is seen in the Horn of Africa in Somalia, where fluvial deposits and playas are found. Topographic and hydrologic erodibility maps show similar strength but different distribution in this region. At the Bodélé depression, we see a more confined hotspot compared to all other erodibility maps. A dust source in Algeria seen in the topographic erodibility map is not present in our map. The land cover map (Figure 2) in this area shows the presence of sand dunes and sand deposits over bedrock, so the apparent dust source could reflect the persistent dust transported by Harmattan winds. The empty areas seen in our erodibility map in the Sahara represent mountains (e.g., the Tibesti Mountains in Chad and the Jebel Marra Mountains in Sudan). Similarly, the mountain ranges in the western Arabian Peninsula, the Hadramaut Mountains in southern Arabian Peninsula, and the Anti-Atlas Mountains in northern Africa are

Table 2. Mean Correlation Coefficients^a and Their Statistics for Different Land Cover Types

Land Cover Types	Mean correlation Coefficient	SD	Min	Max	Total No. of Grid Cells Used
Bedrock, with sediment	0.28	0.06	0.12	0.60	48363
Sand deposit	0.30	0.06	0.12	0.63	30705
Sand deposit, on bedrock	0.28	0.06	0.12	0.51	22763
Sand deposit, stabilized	0.31	0.06	0.15	0.41	3864
Agricultural and urban area	0.31	0.07	0.12	0.67	35591
Fluvial system	0.29	0.06	0.12	0.47	32478
Stony surface	0.26	0.07	0.12	0.44	7165
Playa/Sabkha	0.44	0.15	0.15	0.70	5317
Savanna/Grassland	0.36	0.14	0.15	0.65	29675

^aMean Spearman's rank correlation coefficient (ρ) between ERA-Interim wind at 10 m and MODIS deep blue aerosol optical depth (AOD) at 550 nm, averaged over the entire study area.

correctly represented as nonemitting surfaces in our map. This is generally similar to all topographic, hydrologic, and geomorphic erodibility maps, although the spatial distribution is different. Overall, our erodibility map correctly identifies the major dust sources in the MENA region.

4.3. Erodibility of Land Cover Types

Table 2 lists the mean correlation coefficient and the corresponding standard deviation for each land cover type over the entire study area calculated as discussed in section 3.3. Maximum and minimum correlation coefficients are also reported, which indicates the range of regional variation of erodibility for a given land cover type.

Playa/sabkha has the highest mean correlation coefficient, indicating that it is most erodible among the land cover types. This is consistent with previous findings that playas have the highest dust emission intensity [Cahill *et al.*, 1996; Lee *et al.*, 2011]. The second highest erodible land cover type is savanna/grassland with a mean correlation coefficient of 0.36. Savannas are typically found between south of Sahel and north of the equatorial rainforests. This result indicates that the area may have been highly disturbed, becoming a stronger source of dust. Savannas in this region are characterized by extensive cattle grazing and biomass burning. Both playa/sabkha and savanna/grassland have relatively large standard deviations compared to the rest of the land cover types, indicating that the regional variation of these land cover types as dust source is high. Sand deposit, stabilized, and agricultural and urban area have equal mean correlation coefficients equal to 0.31. We included a mixture of sand dunes and playas in the category sand deposit, stabilized, which explains the observed higher mean correlation coefficient. Lee *et al.* [2011] located the origin of dust plumes using MODIS visible images and found that cultivated sand sheets are the largest sources of dust in West Texas. Sand deposit has a mean correlation coefficient of 0.30, indicating that the sand dunes are also a significant contributor of dust in the study area. Crouvi *et al.* [2012] found that active sand dunes are the most frequent dust sources in Sahara based on the correlation between the frequency of dust storms and the distribution of geomorphic units using high-resolution satellite data. They proposed that aeolian abrasion in sand dunes produces clay-/silt-sized particles by removing the clay coating and breaking the sharp corners. Fluvial system has a mean correlation coefficient of 0.29 indicating that this land cover type has a significant amount of fine sediment suitable for dust emission. Sweeney *et al.* [2011] in a field-based study found that alluvial deposits can have high dust emission potential, comparable to that of playa surfaces. Given higher erodibility of land use than fluvial systems, it may be inferred that the anthropogenic activities aggravate dust emission. In fact, the agricultural and urban area in the MENA region consists of heavily cultivated areas, which are in most cases located in the base of the fluvial system such as valleys. Sand deposit, on bedrock, has a mean correlation coefficient of 0.28, so the dust emission from these areas should not be underestimated. This land cover type mainly includes aeolian deposits on bedrock, which may be remobilized. In North Africa, fine sediment originating from the Libyan and Egyptian deserts are transported and deposited by the northeasterly Harmattan wind in winter. Stony surface has the minimum mean correlation coefficient equal to 0.26, indicating that they are least erodible compared to other land cover types.

5. Discussion and Modeling Perspective

Representation of the spatiotemporal dynamics of dust sources in the models can improve dust-mass flux estimates, which are essential for accurately quantifying the various impacts of dust (e.g., on the Earth's

radiation budget). Use of the proposed dust source framework may improve dust source characterization in the climate models because our approach for erodibility mapping is more physically based. The association of sediment supply with different land cover types is shown by many previous studies [e.g., Bullard *et al.*, 2011; Lee *et al.*, 2011]. Yue *et al.* [2009] also used constant emission potential coefficients of 0.1, 0.3, and 1.0, respectively, for grassland, meadow, and desert, an approach that is not realistic because of the limited number of surfaces and arbitrarily assigned coefficients. We note that the erodibility of a land cover type is regionally variable. For example, playas commonly contain a supply of fine sediment suitable for dust emission, but this quantity of fine sediment may differ from one location to another. We attribute this regional variability of erodibility within the same land cover type to complex localized land-atmosphere interactions, topography, crusting, and vegetation.

The availability-limited condition is generally represented in the models by expressing the threshold friction speed in terms of soil moisture. Given the general unavailability of accurate soil moisture data, the use of a region-specific and temporally adjusted dynamic land cover erodibility map may be necessary for accurate dust source characterization in climate models. Such region-specific, temporally varying erodibility can be specified by combining the land cover map and the monthly dynamic erodibility map presented in this study. This conclusion is also supported by some recent studies [e.g., Kim *et al.*, 2013] that observed improvements in dust emission using a MODIS NDVI (normalized difference vegetation index) based, dynamic dust source function.

We developed the land cover map in high-resolution but we derived the erodibility of the land cover types from a coarser-resolution ($1^\circ \times 1^\circ$) correlation map between surface wind and AOD, which is the main limitation of this study. With our mapping technique, the grouping of transition zones was subjective, another limitation of this study. Dust emission that takes place at smaller scale, such as from savannas, alluvial fans, etc., might not be captured by coarser mapping techniques. So in the areas where multiple land cover types exist within a ($1^\circ \times 1^\circ$) grid cell, the developed erodibility map may not be very accurate. The large range of variation in erodibility indicated by the minimum and maximum correlation (Table 2) suggests such possibility of error. As high-resolution surface wind speed and aerosol optical depth observations become available in the future, smaller-scale dust emission can be captured using the same method adopted in this study. We acknowledge that the erodibility is not solely characterized by land cover type but rather changes continuously in response to the complex feedback between the land cover and atmospheric phenomena. We also note that the erodibility is also linked to the topography, as shown by Ginoux *et al.* [2001]. Creating subtypes within a land cover type based on topographic information could indeed improve our erodibility map. Global land-use pattern has changed greatly because of anthropogenic activities, and it will continue to change. Further, the seasonality of erodibility observed in the 10 years of recent data may not reflect the longer-term dust signals associated with paleoclimatic cycles. If the proposed map is to be used for understanding past and future dust climatology, these issues should be addressed by tuning with paleodust proxies as done by Albani *et al.* [2012].

Working at a finer scale than 1:250,000 would produce a more detailed land cover map, but the process would be tedious and the results less relevant in the current global modeling context. We produced the land cover map at ($0.1^\circ \times 0.1^\circ$) by converting the vector map in ArcGIS into a gridded map with the maximum area method. Because the portion of smaller features within a grid cell is discarded in this conversion process, some error during regridding is unavoidable, but this error reduces with increasing spatial resolution of the map. We believe that the integration of the land cover map into the existing dust/climate models can be done in several other ways. For example, the land cover map could be integrated by specifying threshold friction velocity, clay content, roughness length, and threshold friction speed for each land cover type. Being a digital map of vector polygons, our map has the flexibility to be regrouped and integrated in a desired fashion as necessary.

6. Conclusion

In this paper, we describe a high-resolution land cover map of the Middle East and North Africa (MENA) region that can be used in climate models to characterize the subgrid variability of dust sources. We developed the land cover map by classifying the land cover into 12 categories by visually examining high-resolution satellite images obtained from Google Earth Professional and Environmental Systems Research Institute (ESRI) Basemap. Based on dust emission potential, the erodible land cover types in the MENA region are grouped into nine categories: (1) bedrock: with sediment, (2) sand deposit, (3) sand deposit: on bedrock, (4) sand deposit: stabilized, (5) agricultural and urban area, (6) fluvial system, (7) stony surface, (8) playa/sabkha,

and (9) savanna/grassland. Given the general unavailability of high-resolution data sets of soil and land cover types in the MENA region, this map serves as a baseline for understanding the role of geomorphology in dust emission. We used the correlation between ERA-Interim wind speed at 10 m and MODIS deep blue AOD at 550 nm to quantify the erodibility of the different land cover types. This method of quantifying land cover erodibility improves dust source characterization, especially in the areas of persistent dust transport, biomass burning, and agricultural areas, as compared to existing erodibility maps. Our results also indicate that the erodibility is linked to the land cover type and has regional variation. Association with the land cover types gives the term erodibility a physical basis accounting the sediment supply and the availability of that sediment under a given wind forcing. The combined use of the land cover map and the erodibility map presented in this study can improve dust source characterization in climate models.

Acknowledgments

This work was funded by the third-round grant from King Abdullah University of Science and Technology. MODIS deep blue aerosol optical depth data, GPCP precipitation data, and Angstrom exponent data used in this study were obtained from the Giovanni online data system, developed and maintained by the NASA GES DISC. ECMWF ERA-Interim data used in this study were obtained from the ECMWF data server. NCEP reanalysis data were obtained from <http://www.esrl.noaa.gov/psd/>, a website maintained by the NOAA/OAR/ESRL PSD, Boulder, Colorado, USA.

References

- Albani, S., N. M. Mahowald, B. Delmonte, V. Maggi, and G. Winckler (2012), Comparing modeled and observed changes in mineral dust transport and deposition to Antarctica between the Last Glacial Maximum and current climates, *Clim. Dyn.*, *38*(9–10), 1731–1755, doi:10.1007/s00382-011-1139-5.
- Ballantine, J.-A., G. S. Okin, D. E. Prentiss, and D. A. Roberts (2005), Mapping North African landforms using continental scale unmixing of MODIS imagery, *Remote Sens. Environ.*, *97*(4), 470–483, doi:10.1016/j.rse.2005.04.023.
- Bangert, M., A. Nenes, B. Vogel, H. Vogel, D. Barahona, V. A. Karydis, P. Kumar, C. Kottmeier, and U. Blahak (2012), Saharan dust event impacts on cloud formation and radiation over Western Europe, *Atmos. Chem. Phys.*, *12*, 4045–4063, doi:10.5194/acp-12-4045-2012.
- Bond, T. C., et al. (2013), Bounding the role of black carbon in the climate system: A scientific assessment, *J. Geophys. Res. Atmos.*, *118*, 5380–5552, doi:10.1002/jgrd.50171.
- Bullard, J. E., S. P. Harrison, M. C. Baddock, N. Drake, T. E. Gill, G. McTainsh, and Y. Sun (2011), Preferential dust sources: A geomorphological classification designed for use in global dust-cycle models, *J. Geophys. Res.*, *116*, F04034, doi:10.1029/2011JF002061.
- Cahill, T. A., T. E. Gill, J. S. Reid, E. A. Gearhart, and D. A. Gillette (1996), Saltating particles, playa crusts and dust aerosols at Owens (dry) Lake, California, *Earth Surf. Processes Landforms*, *21*(7), 621–639, doi:10.1002/(SICI)1096-9837(199607)21:7<621::AID-ESP661>3.0.CO;2-E.
- Creamean, J. M., et al. (2013), Dust and biological aerosols from the Sahara and Asia influence precipitation in the Western U.S., *Science*, *339*(6127), 1572–1578, doi:10.1126/science.1227279.
- Crouvi, O., K. Schepanski, R. Amit, A. R. Gillespie, and Y. Enzel (2012), Multiple dust sources in the Sahara Desert: The importance of sand dunes, *Geophys. Res. Lett.*, *39*, L13401, doi:10.1029/2012GL052145.
- Dee, D. P., et al. (2011), The ERA-Interim reanalysis: Configuration and performance of the data assimilation system, *Q. J. R. Meteorol. Soc.*, *137*(656), 553–597, doi:10.1002/qj.828.
- Eck, T., et al. (1999), Wavelength dependence of the optical depth of biomass burning, urban and desert dust aerosols, *J. Geophys. Res.*, *104*(D24), 31,333–31,349, doi:10.1029/1999JD900923.
- Engelstaedter, S., and R. Washington (2007), Atmospheric controls on the annual cycle of North African dust, *J. Geophys. Res.*, *112*, D03103, doi:10.1029/2006JD007195.
- Ginoux, P., M. Chin, I. Tegen, J. M. Prospero, B. Holben, O. Dubovik, and S. J. Lin (2001), Sources and distributions of dust aerosols simulated with the GOCART model, *J. Geophys. Res.*, *106*(D17), 20,255–20,273, doi:10.1029/2000JD000053.
- Ginoux, P., J. M. Prospero, T. E. Gill, N. C. Hsu, and M. Zhao (2012), Global-scale attribution of anthropogenic and natural dust sources and their emission rates based on MODIS deep blue aerosol products, *Rev. Geophys.*, *50*, RG3005, doi:10.1029/2012RG000388.
- Goudie, A. (2013), *Arid and Semi-Arid Geomorphology*, Cambridge Univ. Press, Cambridge.
- Hansen, M. C., R. S. Defries, J. R. G. Townshend, and R. Sohlberg (2000), Global land cover classification at 1 km spatial resolution using a classification tree approach, *Int. J. Remote Sens.*, *21*(6–7), 1331–1364, doi:10.1080/014311600210209.
- Hsu, N. C., S. C. Tsay, M. D. King, and J. R. Herman (2004), Aerosol properties over bright-reflecting source regions, *IEEE Trans. Geosci. Remote Sens.*, *42*(3), 557–569, doi:10.1109/TGRS.2004.824067.
- Intergovernmental Panel on Climate Change (IPCC) (2007), *Climate Change 2007: The Physical Science Basis: Contribution of Working Group I to the Fourth Assessment Report of the IPCC*, edited by S. Solomon et al., pp. 167–180, Cambridge Univ. Press, New York.
- Kalnay, E., et al. (1996), The NCEP/NCAR 40-year reanalysis project, *Bull. Am. Meteorol. Soc.*, *77*(3), 437–471, doi:10.1175/1520-0477(1996)077<0437:TNYRP>2.0.CO;2.
- Kellogg, C. A., and D. W. Griffin (2006), Aerobiology and the global transport of desert dust, *Trends Ecol. Evol.*, *21*(11), 638–644, doi:10.1016/j.tree.2006.07.004.
- Kim, D., et al. (2013), The effect of the dynamic surface bareness on dust source function, emission, and distribution, *J. Geophys. Res. Atmos.*, *118*, 871–886, doi:10.1029/2012JD017907.
- Kocurek, G., and N. Lancaster (1999), Aeolian system sediment state: Theory and Mojave Desert Kelso dune field example, *Sedimentology*, *46*(3), 505–515, doi:10.1046/j.1365-3091.1999.00227.x.
- Koren, I., Y. J. Kaufman, R. Washington, M. C. Todd, Y. Rudich, J. V. Martins, and D. Rosenfeld (2006), The Bodélé depression: A single spot in the Sahara that provides most of the mineral dust to the Amazon forest, *Environ. Res. Lett.*, *1*(1), 014005, doi:10.1088/1748-9326/1/1/014005.
- Lawrence, P. J., and T. N. Chase (2007), Representing a new MODIS consistent land surface in the Community Land Model (CLM3.0), *J. Geophys. Res.*, *112*, G01023, doi:10.1029/2006JG000168.
- Lee, J. A., M. C. Baddock, M. J. Mbuh, and T. E. Gill (2011), Geomorphic and land cover characteristics of aeolian dust sources in West Texas and eastern New Mexico, USA, *Aeolian Res.*, *3*(4), 459–466, doi:10.1016/j.aeolia.2011.08.001.
- Lobeck, A. K. (1946), *Physiographic Diagram of Africa*, Geographical Press, formerly of Columbia University, a division of Hammond, Incorporated, Maplewood, N. J.
- Loveland, T. R., B. C. Reed, J. F. Brown, D. O. Ohlen, Z. Zhu, L. Yang, and J. W. Merchant (2000), Development of a global land cover characteristics database and IGBP DISCover from 1 km AVHRR data, *Int. J. Remote Sens.*, *21*(6–7), 1303–1330, doi:10.1080/014311600210191.
- Mahowald, N. M., D. R. Muhs, S. Levis, P. J. Rasch, M. Yoshioka, C. S. Zender, and C. Luo (2006), Change in atmospheric mineral aerosols in response to climate: Last glacial period, preindustrial, modern, and doubled carbon dioxide climates, *J. Geophys. Res.*, *111*, D10202, doi:10.1029/2005JD006653.

- Matmon, A., O. Simhai, R. Amit, I. Haviv, N. Porat, E. McDonald, L. Benedetti, and R. Finkel (2009), Desert pavement-coated surfaces in extreme deserts present the longest-lived landforms on Earth, *Geol. Soc. Am. Bull.*, *121*(5–6), 688–697, doi:10.1130/B26422.1.
- McTainsh, G. (1980), Harmattan dust deposition in northern Nigeria, *Nature*, *286*(5773), 587–588, doi:10.1038/286587a0.
- Miller, R. L., and I. Tegen (1998), Climate response to soil dust aerosols, *J. Clim.*, *11*(12), 3247, doi:10.1175/1520-0442(1998)011<3247:CRTSDA>2.0.CO;2.
- Oleson, K. W., et al. (2008), Improvements to the Community Land Model and their impact on the hydrological cycle, *J. Geophys. Res.*, *113*, G01021, doi:10.1029/2007JG000563.
- Parajuli, S. P., I. Gherboudj, and H. Ghedira (2013), The effect of soil moisture and wind speed on aerosol optical thickness retrieval in a desert environment using SEVIRI thermal channels, *Int. J. Remote Sens.*, *34*(14), 5054–5071, doi:10.1080/01431161.2013.788262.
- Prospero, J. M., P. Ginoux, O. Torres, S. E. Nicholson, and T. E. Gill (2002), Environmental characterization of global sources of atmospheric soil dust identified with the Nimbus 7 Total Ozone Mapping Spectrometer (TOMS) absorbing aerosol product, *Rev. Geophys.*, *40*(1), 1002, doi:10.1029/2000RG000095.
- Rao, P. G., H. R. Hatwar, M. H. Al-Sulaiti, and A. H. Al-Mulla (2003), Summer shamals over the Arabian Gulf, *Weather*, *58*(12), 471–478, doi:10.1002/wea.6080581207.
- Reid, J. S., E. A. Reid, A. Walker, S. Piketh, S. Cliff, A. Al Mandoos, S.-C. Tsay, and T. F. Eck (2008), Dynamics of southwest Asian dust particle size characteristics with implications for global dust research, *J. Geophys. Res.*, *113*, D14212, doi:10.1029/2007JD009752.
- Schepanski, K., I. Tegen, and A. Macke (2012), Comparison of satellite based observations of Saharan dust source areas, *Remote Sens. Environ.*, *123*, 90–97, doi:10.1016/j.rse.2012.03.019.
- Shao, Y. (2000), *Physics and Modelling of Wind Erosion*, Atmospheric and Oceanographic Sciences Library, vol. 37, Kluwer Acad. Publishers, Dordrecht, Netherlands.
- Sokolik, I. N., and O. B. Toon (1996), Direct radiative forcing by anthropogenic airborne mineral aerosols, *Nature*, *381*(6584), 681–683, doi:10.1038/381681a0.
- Sweeney, M. R., E. V. McDonald, and V. Etyemezian (2011), Quantifying dust emissions from desert landforms, eastern Mojave Desert, USA, *Geomorphology*, *135*(1), 21–34, doi:10.1016/j.geomorph.2011.07.022.
- Torres, O., P. K. Bhartia, J. R. Herman, Z. Ahmad, and J. Gleason (1998), Derivation of aerosol properties from satellite measurements of backscattered ultraviolet radiation: Theoretical basis, *J. Geophys. Res.*, *103*(D14), 17,099–17,110, doi:10.1029/98JD00900.
- Van Pelt, R., M. C. Baddock, T. M. Zobeck, A. J. Schlegel, M. F. Vigil, and V. Acosta-Martinez (2013), Field wind tunnel testing of two silt loam soils on the North American Central High Plains, *Aeolian Res.*, *10*, 53–59, doi:10.1016/j.aeolia.2012.10.009.
- Yue, X., H. Wang, Z. Wang, and K. Fan (2009), Simulation of dust aerosol radiative feedback using the Global Transport Model of Dust: 1. Dust cycle and validation, *J. Geophys. Res.*, *114*, D10202, doi:10.1029/2008JD010995.
- Zender, C. S., D. Newman, and O. Torres (2003), Spatial heterogeneity in aeolian erodibility: Uniform, topographic, geomorphic, and hydrologic hypotheses, *J. Geophys. Res.*, *108*(D17), 4543, doi:10.1029/2002JD003039.
- Zobler, L. (1999), *Global Soil Types, 1-Degree Grid (Zobler), Data Set*. [Available at <http://www.daac.ornl.gov>] from Oak Ridge National Laboratory Distributed Active Archive Center, Oak Ridge, Tenn., doi:10.3334/ORNLDAAAC/418.